Journal of Environmental Chemical Engineering 11 (2023) 109841

Contents lists available at ScienceDirect

Journal of Environmental Chemical Engineering

journal homepage: www.elsevier.com/locate/jece

Co_3O_4 hollow nanotubes for the catalytic oxidation of C_2-chlorinated VOCs

Amaya Gil-Barbarin, José Ignacio Gutiérrez-Ortiz, Rubén López-Fonseca, Beatriz de Rivas *

Chemical Technologies for Environmental Sustainability Group, Department of Chemical Engineering, Faculty of Science and Technology, University of The Basque Country UPV/EHU, Barrio Sarriena s/n, Leioa, E-48940, Spain

ARTICLE INFO

Editor: Fumitake Takahashi

Keywords:
Cobalt oxide
Kirkendall effect
Hollow nanotubes
Catalytic oxidation
Vinyl chloride
1,2-dichloroethane

ABSTRACT

Structured Co_3O_4 catalysts with a hollow nanotube morphology were prepared by several synthesis routes based on the Kirkendall effect. The resulting samples were kinetically evaluated in the gas-phase oxidation of vinyl chloride and 1,2-dichloroethane, two model C_2-chlorinated volatile organic compounds; and exhaustively characterised by means of BET measurements, X-ray diffraction, scanning electron microscopy with energy dispersive X-ray spectroscopy, Raman spectroscopy, X-ray photoelectron spectroscopy, thermogravimetry and temperature-programmed techniques (adsorption of ammonia and chlorinated VOC, O_2-TPD, H_2-TPR and TPO). The performance of the prepared nanotubes was essentially controlled by the presence of active oxygen species at the surface, which in turn depended on the Co^{2+}/Co^{3+} molar ratio, and the adsorption capacity of the catalyst for the chlorocarbon. Both pollutants were efficiently converted to deep oxidation products at relatively low temperatures. In addition, the optimal catalyst exhibited an appreciable stability when operating during 120 h.

1. Introduction

Chlorinated volatile organic compounds (Cl-VOCs) are defined as a widespread group of pollutants characterised by high volatility and toxicity and strong resistance to degradation. Consequently, Cl-VOCs are categorised as highly hazardous emissions in most countries [1,2]. Based on their molecular structure, Cl-VOCs can be classified into three different groups, namely chlorinated alkanes, chlorinated alkenes and chlorinated aromatics [3]. These compounds are emitted to the atmosphere from several sources, most of them anthropogenic. They are used as solvents, cleaning agents, degreasers, air fresheners, herbicides, insecticides, gasoline additives and intermediates for chemical synthesis. However, they can also be naturally generated by fungi and lichens [4]. Their release to the atmosphere has sweeping environmental consequences connected with the increase of photochemical smog, the depletion of stratospheric ozone and the generation of ground-level ozone. Moreover, many Cl-VOCs provoke severe health problems such as damage of the central nervous system, harmful effects in human tissues and organs, and respiratory problems [4,5].

Among the technologies proposed to remove these toxic compounds, catalytic oxidation is highly efficient to eliminate trace amounts (<1%) of Cl-VOCs at low temperatures [6]. The main operational parameter of this strategy is the selection of the suitable catalyst while simultaneously considering cost, activity and selectivity, and stability or durability. Traditionally, noble metals have been used, especially Pt and Pd, deposited on supports with a high surface area (γ-Al_2O_3, SiO_2, zeolites). Despite their appreciable activity in the oxidation of these pollutants, their high cost and sensitivity to chlorine poisoning have provoked the pursuit of cheaper and more stable alternatives [7]. In this sense, non-noble metal oxide catalysts are considered an attractive substitute. Thus far, transition metal oxides (Mn, V, Cu, Fe), bulk or supported, and perovskites have been widely used for the catalytic combustion of chlorinated VOCs. However, even though these systems are known to exhibit notable catalytic activities, they have some drawbacks including deactivation due to chlorine poisoning, formation of undesired reaction by-products or poor durability [8–10]. Interestingly, cobalt oxide catalysts, could overcome these shortcomings due to their excellent redox properties, high oxygen mobility and surface acidity. Indeed, cobalt-based catalysts have been reported to be efficient for the oxidation of a variety of pollutants including methane, nitrogen monoxide, carbon monoxide and propane, among others [11–14].

Over the last few years, nanostructured cobalt-based catalysts with different controlled morphologies have received great attention, as changes in morphology can induce modifications in physical-chemical properties closely related to the catalytic activity. Zhu et al. synthesised Co_3O_4 nanoparticles with different morphologies (rods, flowers, cages and single crystal) and showed that single crystal morphology enlarged surface area, improved low-temperature

* Corresponding author.
E-mail address: beatriz.derivas@ehu.eus (B. de Rivas).

https://doi.org/10.1016/j.jece.2023.109841
Received 19 December 2022; Received in revised form 21 February 2023; Accepted 31 March 2023
Available online 7 April 2023
2213-3437/© 2023 The Authors. Published by Elsevier Ltd. This is an open access article under the CC BY-NC-ND license (http://creativecommons.org/licenses/by-nc-nd/4.0/).

reducibility and increased the amount of active surface species, which resulted in a better performance in the oxidation of ethyl acetate [15]. A similar finding was reported by Liu et al. who evaluated the catalytic efficiency of Co_3O_4 nanospheres in toluene oxidation and found out that morphology was closely related to adsorbed oxygen species, structural defects, reducibility and exposed planes [16]. Furthermore, in addition to a determined morphology, hollow nanotubes provide larger specific surface areas, more accessible active sites, favours rapid mass transport and enhances electron transportation, some highly desirable features in environmental catalysis [17–22]. These cobalt hollow nanostructures, which to the best of our knowledge, have been not examined for the catalytic oxidation of Cl-VOCs, can be obtained through a mechanism named the Kirkendall effect. Briefly, the Kirkendall effect results in the formation of hollow structures without costly templates and corrosive acids, due to the different diffusion rates between two species in a solid. If the diffusion rate of the species heading outward is greater than the diffusion rate of the species diffusing inward, cavities will be generated giving rise to highly defective nanomorphologies [21].

Thus, the motivation of this study lies in examining less conventional Co_3O_4 catalysts with a controlled 1D nanomorphology (hollow nanotubes), obtained by three different synthesis routes based on the Kirkendall effect, for the oxidative gas phase removal of traces amounts (1000 ppm) of C_2-chlorinated VOCs. The physicochemical properties of these oxides were characterised by several techniques including N_2 physisorption, X-ray diffraction (XRD), scanning electron microscopy (SEM), temperature-programmed reduction with hydrogen (H_2-TPR), temperature-programmed desorption of oxygen (O_2-TPD), Cl-VOC and NH_3 adsorption followed by thermogravimetry, X-ray photoelectron spectroscopy (XPS) and Raman spectroscopy. Among the different types of Cl-VOCs, the employment of chlorinated ethanes and ethenes stands out, with an annual production of more than 1000 metric tons per year. This large-scale production and consumption worldwide lead to the release of these compounds into the atmosphere, and they are the most frequently detected organic pollutants in soil and groundwater as well. Moreover, some of these C_2-chlorocarbons have been included as priority hazardous substances by the US Environmental Protection Agency, the Chinese Ministry of Environmental Protection and the European Commission. Specifically, 1,2-dichloroethane (DCE) and vinyl chloride (VC) were chosen as model compounds in this work. These chlorocarbons are important bulk chemical extensively used in the production of polyvinylchloride employed in pipes, packaging materials and wire and cable coatings. DCE is also employed as an industrial solvent and metal degreaser and is commonly used for the synthesis of other chlorinated hydrocarbons such as vinyl chloride, trichloroethane, trichloroethylene and perchloroethylene. On the other hand, other less common uses of VC are automobile upholstery and parts, wall coverings, household goods and furniture [1,23].

2. Experimental

2.1. Preparation of the hollow Co_3O_4 nanotubes

Three types of bulk Co_3O_4 samples with the desired hollow nanotube morphology were synthesised following three simple preparation routes based on the Kirkendall effect. A simplified scheme including the main steps of each procedure is depicted in Fig. 1. All of them essentially involved two main partial objectives, namely the synthesis of a proper catalyst precursor and its thermal transformation to Co_3O_4 under controlled conditions.

2.1.1. Co_3O_4(S) sample

Initially two aqueous solutions of oxalic acid dihydrate (Merck) 0.075 M and cobalt chloride hexahydrate (Alfa Aesar) 0.02 M were mixed under stirring. A pink precipitate ($CoC_2O_4{\cdot}2\,H_2O$) was obtained, which was further aged under stirring for 3 h. This precursor was collected by filtration, thoroughly washed with at least 4 L of water to remove the remaining chlorine species, and dried at room temperature overnight. Afterwards, the product was dispersed in ethanol (VWR

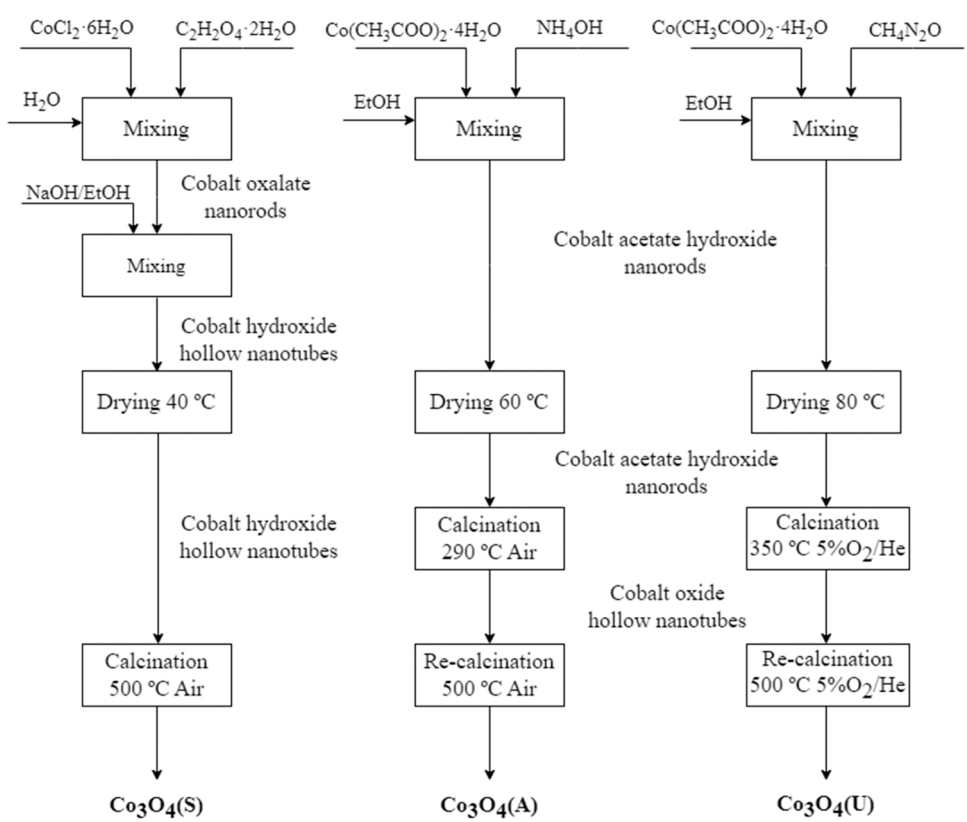

Fig. 1. Scheme of the investigated Kirkendall effect-based synthesis routes.

Chemicals), and an ethanolic solution of NaOH (Merck) 0.1 M was then added drop by drop. With the progressive addition of the caustic solution, the colour of the solution changed from pink to cloudy blue, evidencing the formation of α-$Co(OH)_2$. Then it turned green, and gradually a brown precipitate was obtained that corresponded to the formation of β-$Co(OH)_2$ nanotubes [24]. After 3 h under mechanical stirring, the product was collected by filtration, washed with 10 L of water to eliminate the traces sodium and ethanol, and dried at 40 °C overnight. Finally, the obtained precursor was calcined in static air with a heating ramp of 1 °C min^{-1} and kept for 4 h at 500 °C.

2.1.2. Co_3O_4(A) sample

An aqueous solution of ammonium hydroxide (AppliChem Panreac) 0.02 M was added dropwise to an ethanolic solution of cobalt acetate tetrahydrate (Alfa Aesar) $8{\cdot}10^{-3}$ M under stirring. The precipitate (cobalt hydroxide acetate) was aged for 6 days keeping stirring. Afterwards, the solid was collected by centrifugation, washed with water and ethanol, and dried at 60 °C. Finally, the precursor was calcined in static air at 290 °C during 10 min with a heating ramp of 1 °C min^{-1}. At this temperature, the complete decomposition of the precursor and the formation of Co_3O_4 was expected to be achieved. Then, the catalyst was cooled down to room temperature and re-calcined at 500 °C (1 °C min^{-1}) for 4 h to form hollow Co_3O_4 nanotubes [25].

2.1.3. Co_3O_4(U) sample

The catalyst was prepared by a precipitation route of cobalt acetate tetrahydrate (Alfa Aesar) and urea (Fluka). In a conventional procedure, two ethanolic solutions of cobalt acetate (0.03 M) and urea (0.17 M) were mixed. The mixture was maintained under stirring at a constant temperature of 65 °C for 4 h. The precursor was collected by filtration, washed three times with ethanol (VWR Chemicals) and dried at 80 °C overnight. Afterwards, the precursor was calcined in 5%O_2/He at 350 °C with a heating ramp of 1 °C min^{-1} for 3 h. After a subsequent cooling step at room temperature, the solid was re-calcined at 500 °C for 4 h [26].

2.2. Characterisation techniques

Textural properties of the synthesised oxides were examined by N_2 adsorption-desorption isotherms at − 196 °C with a Micromeritics TRISTAR II 3020 instrument. The specific surface areas of the catalysts were calculated using the BET equation and the mean pore size was determined by applying the BJH method. Before each analysis, the samples were degassed at 200 °C for 10 h with N_2 flow.

Powder X-ray diffraction (XRD) and Raman spectroscopy were used to analyse the structural properties of the catalysts. XRD diffraction patterns were collected on an automatic diffractometer model X′Pert PRO from PANalytical using Cu Kα radiation (λ = 1.5406 Å) and a Ni filter at 40 kV and 40 mA. The measurement conditions have been optimised to an angular range between 5° and 80° at 2θ with a step size of 0.026° and counting time of 498.3 s per step. Phase identification was carried out by comparison of the experimental XRD data with ICDD (International Centre for Diffraction Data) database cards. Raman spectra were taken on a Renishaw InVia Raman spectrometer using a 514 nm laser source (ion-argon laser, Modu-Laser) and a Leica 50 x N Plan lens, scanning from 150 to 800 cm^{-1}. For each analysis, 20 s were employed, and 10 scans were accumulated with 10% of the maximum power in the spectral window (2 mW).

The external morphology of the synthesised oxides was evaluated by means of Scanning Electron Microscopy (SEM). For each measurement, a small amount of powdered sample was taken and deposited on a carbon strip in a sample holder. SEM images were obtained on a Hitachi S-4800 scanning electron microscope with cold cathode field emission gun (FEG) at a working voltage of 10 kV and 5 A. The microscope was equipped with a high-resolution CCD camera.

Redox behaviour of the samples was estimated by temperature-programmed reduction experiments with hydrogen (H_2-TPR). These measurements were conducted on a Micromeritics Autochem 2920 instrument equipped with a TCD detector. Prior to analysis, a pretreatment of the sample was carried out in a 5%O_2/He stream at 300 °C for 1 h and then cooled down to room temperature. Afterwards, 50 cm^3 min^{-1} of a 5%H_2/Ar mixture was made to flow through the catalyst bed located in a U-shaped quartz reactor, from room temperature to 500 °C. The heating rate was 10 °C min^{-1} and was maintained at 500 °C for 0.5 h. A cold trap was used in order to prevent water generated by the reduction step from interfering with the TCD detector. In order to examine the nature and mobility of the oxygen species O_2-TPD experiments were also conducted on the Micromeritics Autochem 2920 instrument. On this occasion the outflow was analysed by a Hiden HPR 20 EGA mass spectrometer. Before the analysis, the sample (100 mg) was pre-treated in 5%O_2/He stream at 500 °C for 15 min and the cooled down to 50 °C. Next, after being purged with helium for 30 min, the catalyst was heated to 900 °C for 0.5 h with a heating ramp of 10 °C min^{-1} while following the signal of the desorbed oxygen ($m/z = 32$).

The overall acidity of the catalysts was evaluated by the adsorption of NH_3 at low temperature (100 °C) followed by thermogravimetry. This experiment was carried out on a Setaram Setsys Evolution thermobalance equipped with a cylindrical graphite furnace and integrated PID temperature control. The thermobalance was coupled to a Pfeiffer Vacuum DUO 2.5 mass spectrometer. For each analysis, 80 mg of the sample were weighted and pre-treated in a He stream (50 cm^3 min^{-1}) at 500 °C for 0.5 h with a heating rate of 10 °C min^{-1}. After cooling at 100 °C, a stream of 10%NH_3/He was introduced for 1 h to achieve ammonia adsorption up to saturation. Next, the sample was exposed to a flow of 50 cm^3 min^{-1} of He for 2 h at 100 °C to remove reversibly bound ammonia from the surface. The total acidity of the samples was calculated from the mass gain after the desorption process of the physisorbed ammonia.

On the other hand, and also employing thermogravimetric analysis, the adsorption capacity of both chlorinated molecules was examined. For each analysis, 20 mg of the sample were weighted and pre-treated in an air stream (50 cm^3 min^{-1}) at 500 °C for 0.5 h with a heating rate of 10 °C min^{-1}. Then, the catalyst was cooled to 100 °C. Next, a stream of 5%VC or DCE/air was introduced for 1 h to achieve chlorinated compound adsorption up to saturation. The sample was exposed to a flow of 50 cm^3 min^{-1} of air for 2 h at 100 °C to remove reversibly bound VC/DCE from the surface.

X-ray Photoelectronic Spectroscopy (XPS) measurements were performed on a Kratos AXIS Supra spectrometer using a 120 W Al Kα monochromatic radiation source with a pass energy of 160 eV for the general survey and 20 eV for the specific spectra. The spectra were adjusted using CasaXPS 2.3.16 software, which models Gauss-Lorentzian contributions, after a background subtraction (Shirley). The concentrations were calculated by correcting the values with relative atomic sensitivity factors (Scofield).

The chlorine accumulation and coke formation of the used catalysts were examined by X-ray Energy Dispersive Spectroscopy (EDS) and Temperature Programmed Oxidation (TPO) respectively. EDS results were obtained on a Carl Zeiss EVO-40 scanning electron microscope coupled to EDS microanalysis equipment X-Max from Oxford Instruments. The samples were fixed in an aluminium sample holder by means of a double layer of conductive graphite adhesive and placed inside the microscope under high vacuum. The EDS spectra were measured at 30 kV and 180 pA, working distance of 8.5 mm and X-ray absorption time of 250 s. TPO analyses were conducted in the Setaram Setsys Evolution thermobalance connected to a mass spectrometer. Previously to the oxidation process, all the samples (80 mg) were pretreated in a 5%O_2/He flow at 110 °C for 1 h. Subsequently, the temperature was increased to 800 °C with a heating rate of 10 °C min^{-1} and this temperature was held for 0.5 h.

2.3. Catalytic activity determination

The catalytic behaviour of the catalysts was evaluated in a bench-scale fixed bed reactor (MICROACTIVITY-Reference MAPXL1M6 model, provided by PID Eng&Tech S.L.) fully monitored by computer. For each experiment, the catalytic bed consisted of 0.85 g of catalyst with particle size 0.08–0.16 mm diluted up to 2 mL with inert quartz with particle size 0.5–0.8 mm. The catalyst was placed in a reactor made of quartz with an internal diameter of 10 mm and a height of 300 mm, and a K type thermocouple was set inside to control the temperature. The feed stream consisted of 1000 ppm of the chlorinated hydrocarbon (VC or DCE) diluted in a flow of 500 cm^3 min^{-1} of dry air. The weight and gas hourly space velocities were 35000 mL g^{-1} h^{-1} and 15000 h^{-1}, respectively. When the chlorinated hydrocarbon was liquid DCE, it was injected into the feed stream using a syringe pump (kdScientific 200). The position of liquid injection was electrically heated so as to ensure the complete evaporation of the reactant. Before reaching the catalytic bed, the reaction feed was homogenised in a 2 L mixer, to avoid possible fluctuations in the concentration of the inlet. Catalytic activity was measured from 150 to 500 °C in steps of 25 °C, and conversion data was taken at steady state, typically after 30 min on stream. For the analysis of hydrogen chloride and molecular chlorine both potentiometry and volumetric methods were used, respectively. Further details on analytical procedures are described elsewhere [27].

3. Results and discussion

3.1. Physical-chemical characterisation

Textural properties of the synthesised samples were examined by means of nitrogen physisorption. The adsorption/desorption isotherms of the oxides and the pore size distributions are shown in Fig. S1, Supplementary Material. All the samples exhibited type IV isotherm characteristic of mesoporous solids with type H1 hysteresis loops at a relative pressure of $P/P_0 = 0.85$ due to capillary condensation that occurs in uniform cylinder-shaped pores [28]. The pore size distribution of the Co_3O_4 oxides was bimodal distribution. Thus, small pores around 22 Å were owing to the inner structure of the nanoparticles meanwhile the larger pores around 240, 320 and 340 Å for Co_3O_4(S), Co_3O_4(A) and Co_3O_4(U), respectively, were caused by the aggregation of the nanoparticles [29]. Results of BET surface area, pore volume and pore mean diameter are summarised in Table 1. The Co_3O_4(U) sample exhibited the largest surface area (19 m^2 g^{-1}), followed by Co_3O_4(S) and Co_3O_4(A) oxides, with 16 and 11 m^2 g^{-1}, respectively. Less obvious differences were noticed as for their pore volume, ranging between 0.04 and 0.07 cm^3 g^{-1}. Similarly, a slightly smaller mean pore size was found for the Co_3O_4(U) sample catalyst (200 Å) compared with 250 Å over the other two counterparts.

The X-ray diffraction patterns of the obtained Co_3O_4 catalysts after thermal activation at 500 °C for 4 h are presented in Fig. 2. The three samples showed diffraction peaks at 2θ= 19.0°, 31.3°, 36.9°, 38.5°, 44.8°, 55.7°, 59.4° and 65.2°, which could be assigned to (111), (220), (311), (222), (400), (422), (511) and (440) crystal planes of the cubic Co_3O_4 spinel structure (ICDD 00–042–1467) irrespective of the synthesis route. It is relevant to highlight that no diffraction peaks corresponding to CoO neither other impurities (for example, CoO(OH) species) were detected. Together with the diffractograms of the final oxides, the patterns of the catalytic precursors are also included in Fig. 2. Thus, the formation of the expected intermediates solids for each of the synthesis procedures was verified. For Co_3O_4(S), the $CoC_2O_4 \cdot 2\,H_2O$ phase (ICDD 00–025–0250) was generated after reacting cobalt chloride and oxalic acid, meanwhile the intermediate precursor formed during the synthesis of Co_3O_4(A) and Co_3O_4(U) samples was cobalt acetate hydroxide (ICDD 00–022–0582). After calcination (500 °C), all the obtained catalysts were crystalline Co_3O_4 regardless the followed synthesis route. The average crystallite size was calculated applying the Scherrer equation to the diffraction peak associated with the (311) crystal plane (Table 1). The Co_3O_4(U) oxide showed the smallest crystallite size (22 nm). Appreciably larger crystallites were found for the other two samples (45–72 nm).

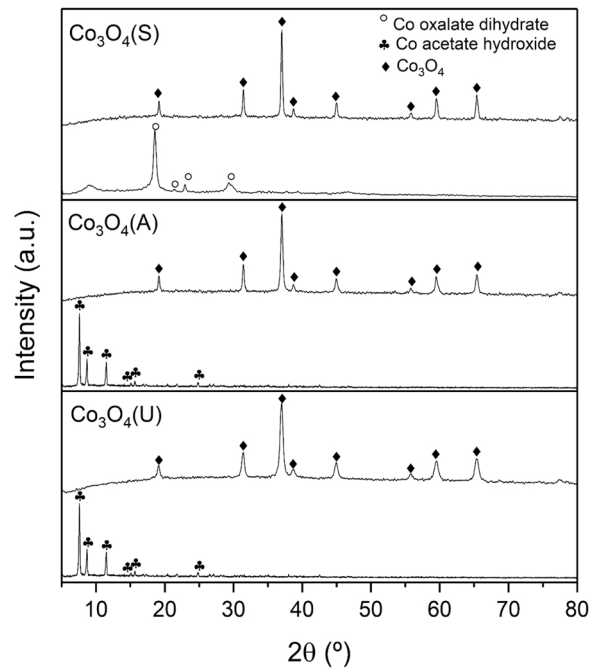

Fig. 2. XRD patterns of the Co_3O_4 samples.

Fig. 3 includes SEM images of the various cobalt precursors that were progressively formed for each of the examined routes based on the Kirkendall effect, and of the thermally-stabilised (500 °C) Co_3O_4 catalysts. These images revealed differences in the morphology of the samples depending on the synthesis method. Images a-d, e-f, and g-i correspond to the Co_3O_4(S), Co_3O_4(A) and Co_3O_4(U) catalysts, respectively. Fig. 3(a) presents the desired compact CoC_2O_4 filamentous morphology, which, after the addition of NaOH, was transformed into β-$Co(OH)_2$ nanotubes (Fig. 3(b)). During the substitution of $CoC_2O_4 \cdot 2\,H_2O$, the Co^{2+} (in CoC_2O_4) and OH^- ions constitute a diffusion pair. The reaction/diffusion process at the solid-liquid interface gives rise to a rapid formation of an $Co(OH)_2$ shell on the external surface of the CoC_2O_4 nanorods, which avoids a direct reaction between CoC_2O_4 and the OH^- species. Therefore, a later reaction depends on the diffusion rates of Co^{2+} and OH^- ions through the $Co(OH)_2$ shell. The generation of

Table 1
Textural, structural and redox properties of the Co_3O_4 catalysts.

Catalyst	S_{BET}, m^2 g^{-1}	V_{pore}, cm^3 g^{-1}	d_{pore}, Å	$D_{Co_3O_4}$, nm	Cell parameter, Å	Relative H_2 uptake at low and high temperature	Bulk Co^{2+}/Co^{3+} molar ratio	O_2 desorbed at low temperature, mmol g^{-1}
Co_3O_4(S)	16	0.07	250	72	8.0608	0.32	0.53	0.038
Co_3O_4(A)	11	0.04	250	45	8.0596	0.39	0.43	0.033
Co_3O_4(U)	19	0.05	200	22	8.0683	0.26	0.64	0.041

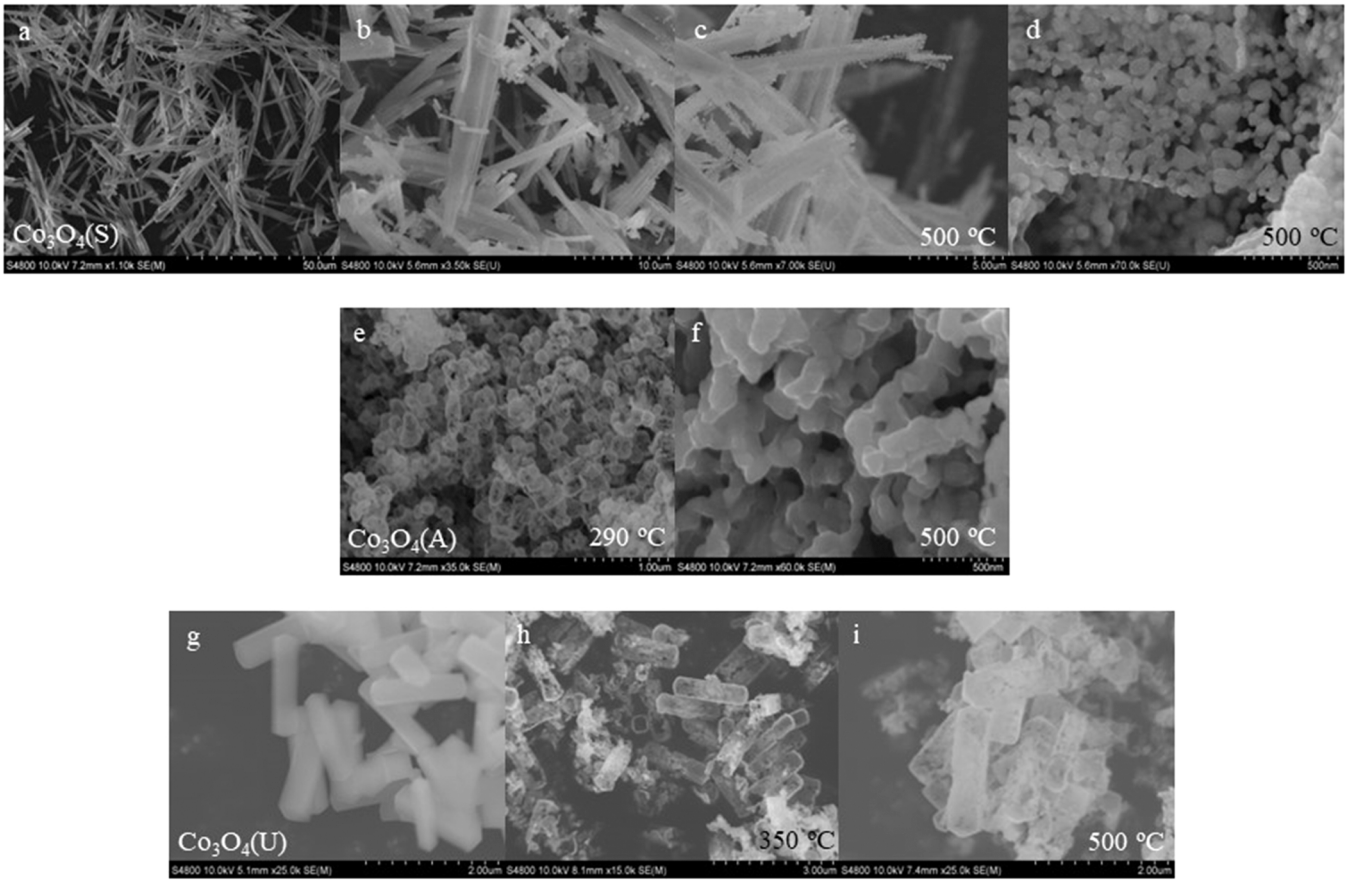

Fig. 3. SEM images of the Co_3O_4 samples before (a-b, g) and after calcination at 500 °C (c-d, e (290 °C)-f, h (350 °C)-i)).

internal vacancies occurs due to an outward flow of Co^{2+} ions through the $Co(OH)_2$ shell, as Co^{2+} ions diffuse faster than OH^- ions. These voids are the origin of the production of the hollow $Co(OH)_2$ nanotubes [21]. Finally, after calcination at 500 °C a phase transformation to Co_3O_4 hollow nanotubes, with a length around 10–15 μm, occurred (Fig. 3(c)). It is worth noting that the walls of the nanotubes were formed by the assembly of particles of irregular particle size ranging between 50 and 200 nm (Fig. 3(d)). On the other hand, the cobalt precursor of Co_3O_4(A) sample exhibited a relatively uniform prism morphology that led to hollow nanotubes after calcination at 290 °C (Fig. 3(e)). For both Co_3O_4(A) and Co_3O_4(U) samples, the hollow structure was achieved in the oven during the slow annealing process. During the heating process, the oxidation of the C, H and Co atoms of the Co acetate hydroxide occurred first on the surface of the precursor. In this way, a film of Co_3O_4 was formed on the surface and the newly exposed C, H and Co atoms emigrated to the surface to react with the oxygen. This process was repeated with the continuous outflow to the surface of the cobalt acetate hydroxide, resulting in the formation of cavities and the subsequent generation of the hollow Co_3O_4 nanotubes [22,30]. It must be pointed out that this regular morphology partially collapsed after calcination at 500 °C (Fig. 3(f)). Similarly, the Co_3O_4(U) precursor was a solid nanoprism (Fig. 3(g)), which after the annealing process (350 °C) became hollow (Fig. 3(h)). In this case its nanotube morphology was well preserved after the re-calcination step at high temperature (Fig. 3(i)). These nanotubes were approximately 1–2 μm in length [26]. In view of the structural, textural and morphological results it could be stated that, although the three synthesised samples were Co_3O_4, only two of them presented the desired high-surface nanotube morphology.

It is widely accepted that the activity of Co_3O_4-based catalysts for oxidation reactions is mostly influenced by the abundance of highly mobile oxygen species. For this purpose, H_2-TPR and O_2-TPD studies are useful for characterising their redox properties and oxygen mobility. Fig. 4 shows the corresponding profiles of the as-synthesised samples in the 100–500 °C temperature range. The observed H_2 uptake occurred between 200 and 400 °C in all cases. No further reduction of the samples

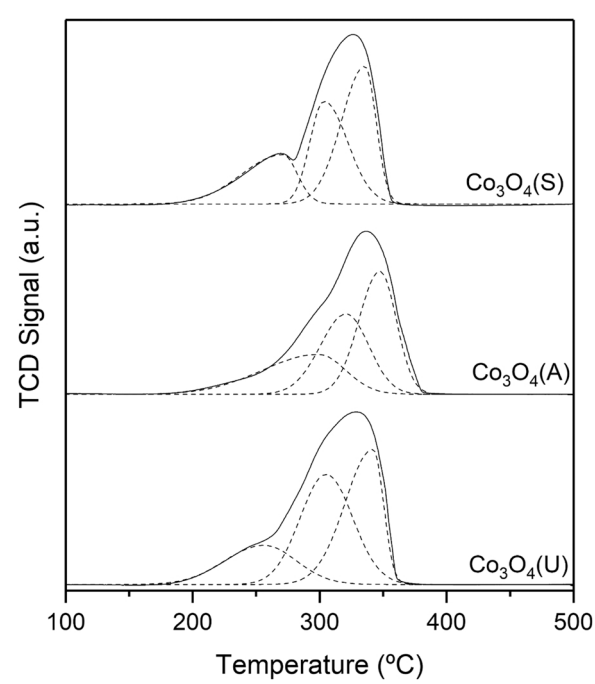

Fig. 4. H_2-TPR profiles of the Co_3O_4 catalysts.

was evident above 400 °C. The traces were dominated by a large consumption at about 330 °C, and a relatively well discernible uptake at 250–300 °C. This redox behaviour is typically associated with a two-step reduction process involving the transformation of Co^{3+} to Co^{2+} (at low temperatures) and Co^{2+} to Co^{0} (at high temperatures) [11,31]. Given the shape of the experimental profiles, an asymmetrical Gaussian model was used to reliably estimate the total H_2 uptake of the samples as well as the relative consumption corresponding to each reduction step. It was found that, within the experimental error, the observed uptakes (16.5–16.8 mmol H_2 g^{-1}) coincided with the theoretical consumption (16.6 mmol H_2 g^{-1}) and the average Co oxidation state (8/3 +). After deconvolution, three reduction contributions were distinguished. Thus, the low-temperature uptake peaked at 260–270 °C over the Co_3O_4(U) and Co_3O_4(S) samples, and at 300 °C for the Co_3O_4(A) sample. Since the conversion of Co^{2+} to metallic cobalt was the dominant reaction in the whole reduction process, experimental results were best fitted to two contributions for quantification purposes. The observed peak temperatures for both Co_3O_4(U) and Co_3O_4(S) samples were comparable (330 °C) while slightly higher temperatures were required over the Co_3O_4(A) sample (340 °C). These findings suggested a poorer reducibility for the latter oxide. Furthermore, when comparing the reducibility of the Co_3O_4(U) and Co_3O_4(S) samples with cobalt oxide catalysts prepared by conventional routes, namely precipitation, sol-gel or hydrothermal method, the temperature of the first reduction peak was 60–100 °C lower [31]. This evidenced that the hollow nanotube morphologies studied in this work significantly enhanced the mobility of oxygen species. Likewise, this nanotube morphology exhibited significantly better redox properties than other nanostructured cobalt oxide catalysts such as nanorods (temperatures for H_2 peak consumption at 285/360 °C) [32] and nanocubes (low-temperature reducibility peak at 270 °C) [33].

It was found that the ratio between the amount of H_2 assigned to the first and the second reduction steps was 0.32 for the Co_3O_4(S) oxide, very close to the theoretical value of 0.33. Interestingly, this ratio was appreciable lower (0.26) for the Co_3O_4(U) sample, thereby evidencing a larger abundance of Co^{2+} species [34]. By contrast, the ratio for the third counterpart (Co_3O_4(A)) was higher (0.39), with a notable relative contribution of Co^{3+} cations. From the estimated H_2 uptakes the corresponding bulk Co^{2+}/Co^{3+} molar ratios of the oxides could be also determined. Details on this calculation are given in Supplementary Material. Taking the theoretical value (0.5) as a reference, the ratio increased from 0.43 (Co_3O_4(A)) to 0.53 and 0.64 (Co_3O_4(S) and Co_3O_4(U), respectively). The enrichment in Co^{2+} species was also observed to be coherent with a marked enlargement of the cell size of the spinel lattice based on the larger ionic radius of Co^{2+} (73 pm) in comparison with Co^{3+} (52 pm) [35]. Thus, the cell parameter (Table 1) progressively increased from 8.0596 Å (Co_3O_4(A)) to 8.0683 Å (Co_3O_4(U)), in fairly good agreement with the larger population of Co^{2+} species. Accordingly, the presence of Co^{2+} species is usually connected to the formation of low coordination defect lattice oxygen sites [36]. To confirm this assumption, the synthesised samples were examined by Raman spectroscopy. Thus, the spectra included five bands in the 100–800 cm^{-1} range, at 187–189, 462–472, 506–515, 597–611 and 664–681 cm^{-1} (Fig. S2, Supplementary Material). These signals corresponded to the F^1_{2g}, E_g, F^2_{2g}, F^3_{2g} and A_{1g} modes of crystalline Co_3O_4, respectively [14]. Interestingly, the relative comparison of the location of the A_{1g} band for the various prepared samples can be taken as an additional evidence for assessing the lattice distortion or residual stress of the spinel structure. More specifically, a shift towards lower frequencies is related to a highly defective structure [14]. Consistently, the location of the A_{1g} band moved from 681 cm^{-1} (Co_3O_4(A)) to 664 cm^{-1} (Co_3O_4(U)).

To further investigate the surface and bulk oxygen species, O_2-TPD measurements were carried out in the 50–900 °C temperature range. The results showed several oxygen desorption peaks attributed to different kinds of oxygen species. Typically, the desorption peaks below 700 °C are related to surface oxygen species, meanwhile the peak above 700 °C is attributed to the desorption of bulk lattice oxygen species [37]. Fig. 5 displays O_2-TPD profiles for all the Co_3O_4 catalysts prepared in this work. The three samples exhibited two overlapping desorption peaks between 120 and 150 °C. It is noteworthy that these were better discernible and with significantly higher peak intensities over the Co_3O_4(U) catalyst, indicating the largest amount of surface oxygen vacancies in this sample. On the other hand, surface lattice oxygen desorbing temperature shifted to higher temperatures from 490 °C over the Co_3O_4(U) and Co_3O_4(S) samples to 530 °C for the Co_3O_4(A) catalyst. The amounts of desorbed surface oxygen species were estimated by integrating the areas of the desorption peaks (Table 1). The Co_3O_4(U) sample desorbed the highest amount of oxygen (0.041 mmol g^{-1}) followed by the Co_3O_4(S) and the Co_3O_4(A) catalysts (0.038 and 0.033 mmol g^{-1}, respectively). These results suggested that the surface oxygen mobility in the Co_3O_4(U) catalyst was appreciably better compared with that of the other samples. Overall, the nanotube morphology, particularly that of Co_3O_4(U) sample, was characterised by a favoured presence of Co^{2+} that ultimately resulted in oxides with a large number of oxygen vacancies or defects and a promoted mobility of oxygen species at low temperature. All these features were expected to be of interest for achieving notable catalytic performances in chlorocarbon combustion.

On the other hand, the effective participation of oxygen species for Cl-VOC destruction requires the previous adsorption of the chlorinated pollutant, mainly on the acid sites of the catalyst [31,36]. In our study the overall acidity of the three cobalt oxides was determined from the net weight gain recorded after an isothermal adsorption step (100 °C) followed by removal of physisorbed ammonia with an inert stream (Table 2). The higher overall acidity was exhibited by the Co_3O_4(S) and Co_3O_4(U) samples, namely 110 and 112 μmol NH_3 g^{-1}, respectively, whilst a considerably lower acidity was found for the Co_3O_4(A) oxide (59 μmol NH_3 g^{-1}). However, when the acid density was compared, the differences among the oxides were less evident (6.7, 5.7 and 5.9 μmol NH_3 m^{-2} for the Co_3O_4 (S), Co_3O_4(A) and Co_3O_4(U) samples, respectively). This finding pointed out that the total acidity was essentially controlled by the surface area of the oxides. As a first approach to the study of the surface reactivity of the catalysts for deep oxidation reactions, the decomposition of the adsorbed probe molecule with increasing temperature under inert conditions was examined. This analysis was carried out by a combined study of the evolution of the weight loss and the composition of the exit stream by mass spectrometry when increasing the temperature from 100 to 500 °C (10 °C min^{-1}) and then maintaining this temperature for 1 h. This investigation could be helpful in evidencing the participation of the oxygen species present in the samples, and thus to compare their relative activity for the oxidative decomposition of ammonia. Fig. 6 includes the corresponding derivative thermogravimetric curves and mass spectra. The following (m/z) MS signals were recorded, namely 15 (NH_3), 18 (H_2O) (not shown), 28 (N_2), 30 (NO, N_2O or NO_2), 44 (N_2O) and 46 (NO_2).

The global picture of the results evidenced that the observed weight loss under dynamic conditions was always larger than the measured weight gain during the NH_3 adsorption step. This difference was necessarily assigned to the consumption of oxygen species from the cobalt oxides, thereby participating in the oxidation of adsorbed ammonia. Indeed, the presence of ammonia in the exit gaseous stream was virtually negligible judging from the flat profiles of the $m/z = 15$ signal. This suggested that, irrespective of the Co_3O_4 catalyst, the extent of the NH_3 desorption process with increasing temperature was very small. From the thermogravimetric measurements it was estimated that the amount of consumed oxygen species gradually increased from 41 μmol O_2 g^{-1} (Co_3O_4(A)), to 63 μmol O_2 g^{-1} (Co_3O_4 (S)) and 117 μmol O_2 g^{-1} (Co_3O_4(U)). These results clearly evidenced a superior oxygen mobility for the Co_3O_4(U) nanotubes with respect to other two counterparts. Furthermore, the relative O_2 consumption/adsorbed NH_3 molar ratio varied from 0.53 (Co_3O_4(S)) to 1.04 (Co_3O_4(U)).

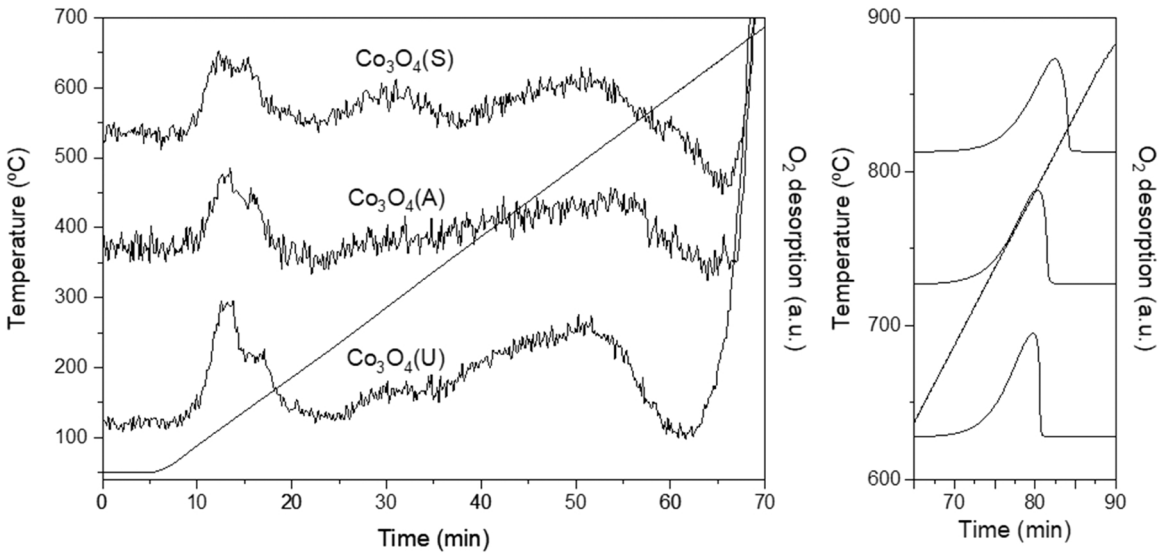

Fig. 5. O_2-TPD profiles of the Co_3O_4 catalysts.

Table 2
Total acidity, amount of active oxygen species, Cl-VOC adsorption capacity and surface composition of the Co_3O_4 catalysts.

Catalyst	Overall acidity, μmol NH_3 g^{-1}	O_2 uptake, μmol g^{-1}	Cl-VOC adsorption capacity, μmol g^{-1}		Co^{2+}/Co^{3+} molar ratio (XPS)	O_{ads}/O_{latt} molar ratio (XPS)
			DCE	VC		
Co_3O_4(S)	110	63	5.7	5.8	0.61	0.61
Co_3O_4(A)	59	41	5.2	2.4	0.60	0.59
Co_3O_4(U)	112	117	11.6	15.0	0.64	0.63

The N-containing products present in the exit stream included N_2, NO, and N_2O [38,39]. The occurrence of the respective oxidation reactions and their favoured selectivity clearly depended on the temperature and the oxygen requirements (O_2/NH_3 stoichiometry). At relatively low temperatures (200 °C) the formation of N_2 ($m/z = 28$) was noticed as the main oxidation product ($4NH_3 + 3\ O_2 \rightarrow 2\ N_2 + 6\ H_2O$). Simultaneously, N_2O ($m/z = 44$, and $m/z = 30$ as well) was detected ($2NH_3 + 2\ O_2 \rightarrow N_2O + 3\ H_2O$). Since the profile of this signal was identical in shape to that observed for the ($m/z = 30$) signal, the latter was also associated with the presence of N_2O. Apparently the activity in the oxidative conversion of ammonia at low temperatures was higher for the Co_3O_4(U) sample, in terms of both the extent of the reaction and peak oxidation temperature. At 300–400 °C the presence of NO as oxidation product ($4NH_3 + 5\ O_2 \rightarrow 4NO + 6\ H_2O$), followed by the ($m/z = 30$) signal, was also evident. Note that the formation of NO_2 ($2NH_3 + 7\ O_2 \rightarrow 2NO_2 + 3\ H_2O$) was negligible as the ($m/z = 46$) signal was virtually flat in the whole temperature range [38].

The capacity of the catalysts for the adsorption of the chlorinated feed was investigated by thermogravimetry. Hence, after a saturation step with a gaseous stream containing 5%Cl-VOC/air followed by a subsequent removal of the reversibly bound VOC, the gain weight at 100 °C was measured. The corresponding results are included in Table 2. Irrespective of the type of compound the Co_3O_4(U) catalyst showed the highest affinity for both Cl-VOCs with adsorption capacities of 11.6 (DCE) and 15 (VC) μmol g^{-1}, considerably higher than that of the other two counterparts (2.4–5.8 μmol g^{-1}). These results were coherent with, on one hand, the lower molecular size of VC (5.6 Å) compared with DCE (6.7 Å), and on the other hand, the high surface area of this sample. On the basis of the fact that efficient VOC removal markedly depends on the total acid sites of the oxides, and in view of the similar overall acidity of Co_3O_4(S) and Co_3O_4(U) catalysts, it could be deduced that the accessibility of the acid sites for VOC chemisorption is better for the Co_3O_4(U) sample.

The composition and chemical state of the surface of the prepared bulk oxides were investigated by XPS analysis. Fig. 7 includes the $Co2p_{3/2}$ and O1s XPS spectra of the oxides. The $Co2p_{3/2}$ profile could be decomposed into five peaks, three spin-orbit doublets at binding energies of 779.8, 780.8 and 781.9 eV, and two peaks of lower intensity at 783.8 and 789.5 eV, which were characteristic shake-up satellites of CoO and Co_3O_4 respectively [38]. The signal at 779.8 eV was ascribed to surface Co^{3+} species in octahedral sites while the contribution at 780.8 eV was assigned to surface Co^{2+} species in tetrahedral sites [40, 41]. The presence of CoO species was dictated by the signal at 781.9 eV, and their contribution in all samples was estimated to be lower than 20% of the total amount of cobalt. It should be pointed out that this species was most likely formed by reduction under vacuum condition in the XPS chamber. On the other hand, the O1s spectra was characterised by a broad peak that suggested the coexistence of several types of surface oxygen species with varying chemical states. It could be deconvoluted into four peaks at 530.0, 530.8, 531.9 and 532.9 eV. The peak at 530.0 eV was correlated to lattice oxygen (O^{2-}, O_{latt}) species, meanwhile band at 530.8 eV was attributed to adsorbed oxygen species on the surface (O^-, O_{ads} species). The bands at 531.9 eV and 532.9 eV were correlated with the presence of adsorbed carbonates and water, respectively [42,43]. The Co^{2+}/Co^{3+} and O_{ads}/O_{latt} molar ratios for the samples are shown in Table 2. Thus, the highest molar ratios were observed for the Co_3O_4(U) sample, namely 0.64 for Co^{2+}/Co^{3+} and 0.63 for O_{ads}/O_{latt}. Besides, it was found that the population of adsorbed oxygen species on the surface was ruled by a larger proportion of Co^{2+}, that is, by a higher Co^{2+}/Co^{3+} ratio [33]. These findings evidenced the beneficial role of Kirkendall effect in forming oxygen vacancies on the surface of the hollow nanotubes of the Co_3O_4(U) catalyst.

3.2. Catalytic behaviour of the Co_3O_4 catalysts

The catalytic efficiency of the as-synthesised Co_3O_4 samples was determined by evaluating the evolution of the conversion of the C_2-chlorinated feed (VC or DCE) to CO_2 with the temperature. The light-off curves are shown in Fig. 8 and the corresponding values of T_{50} and T_{90} (temperatures at which 50% and 90% conversion were attained) are summarised in Table 3. The studied bulk catalysts showed a reasonably good performance since in all cases the pollutant was completely oxidised (>90% conversion to CO_2) below 350 °C and 425 °C for VC and

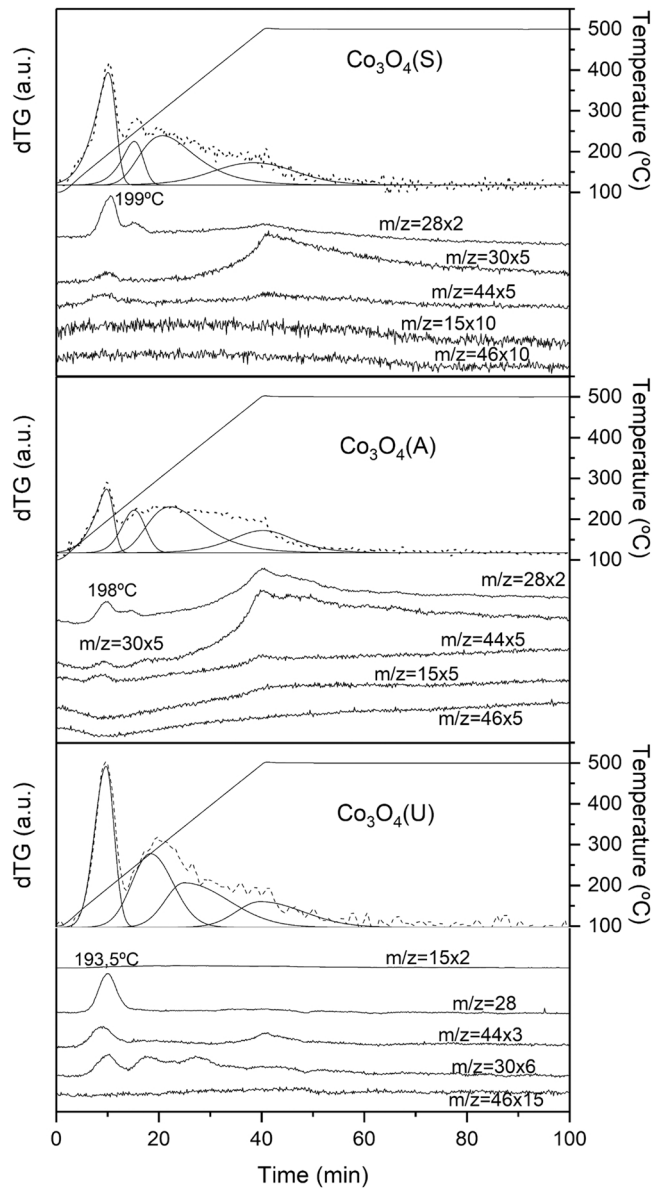

Fig. 6. Derivative thermogravimetric curves and product distribution during the dynamic heating under inert conditions of the Co_3O_4 catalysts saturated with ammonia.

DCE, respectively. It must be highlighted that conversion of both chlorocarbons in the absence of any catalyst was lower than 50% at 550 °C. It was noticed that vinyl chloride was always more easily converted in comparison with DCE over the three cobalt oxides. More particularly, T_{50} and T_{90} values were in the 265–290 °C and 315–345 °C ranges for VC, significantly lower than 325–345 °C and 375–415 °C observed for DCE. The higher reactivity of this chlorinated olefin was in line with the results by Sun et al. [44], who reported that VC oxidation required lower temperatures (30–70 °C) than DCE combustion over Cr_xTi_{1-x} catalysts.

Likewise, substantial differences in catalytic performance were clearly evident depending on the nanostructure of the oxide, thus revealing that the preparation method was a key factor for obtaining a highly active Co_3O_4 catalyst. Among the three investigated oxides, the Co_3O_4(U) sample exhibited the highest efficiency for the oxidative removal of the two chlorinated hydrocarbons. Judging from the results given by the exhaustive characterisation of the samples, the best performance of these hollow nanotubes with a relatively high surface area could be related by the favoured presence of Co^{2+} in the spinel structure, both at surface and bulk level. This in turn led to the formation of low coordination defect lattice oxygen sites that activated the oxidative decomposition of the chlorocarbon by the participation of adsorbed oxygen species. Besides, this oxide presented the largest overall acidity, thus providing a higher amount of sites for the efficient adsorption of the chlorinated compound, and eventually an optimal combination of redox and acid sites in this catalyst.

To clarify these structure-activity relationships the specific reaction rate of the oxides was calculated under differential conditions (when conversion was below 20%). In the case of VC, the estimation was made at 225 °C, while a slightly higher temperature (275 °C) was selected for DCE. The corresponding results are listed in Table 3. The Co_3O_4(U) sample exhibited the highest reaction rate for both chlorinated VOCs (0.23 $mmol_{Cl\text{-}VOC}\ g^{-1}\ h^{-1}$ for VC at 225 °C and 0.29 $mmol_{Cl\text{-}VOC}\ g^{-1}\ h^{-1}$ for DCE at 275 °C). Note that the catalytic activity trend was the same as that dictated by the light-off curves. Fig. 9 evidences a good correlation among the intrinsic reaction rate, the amount of active oxygen species (as estimated from the oxidative decomposition of ammonia and by XPS) and the surface Co^{2+}/Co^{3+} molar ratio (as determined by XPS). As previously demonstrated, a high surface concentration of cobalt in low oxidation state (Co^{2+}) could be an indication of oxygen defects close to the surface. Hence, the abundance of oxygen deficiencies promoted the activation of gas-phase oxygen molecules for the generation of active oxygen species. Furthermore, the key role played by surface oxygen species was also corroborated by the strong relationship between the catalytic activity and the amount of desorbed oxygen at low temperatures estimated by O_2-TPD analysis of the samples (Fig. S3, Supplementary Material). On the other hand, a clear dependence of the specific activity with the Cl-VOC adsorption capacity was also observed, thereby pointing out that the Co_3O_4(U) sample suitably combined physical-chemical features favouring the efficient chemisorption and subsequent attack by reactive oxygen species present in these hollow nanotubes. As for the acid properties, it seemed that overall acidity was a catalytic property of secondary importance since, although the less acid Co_3O_4(A) sample was the oxide with the poorest activity, the other two oxides exhibiting a relatively similar total acidity showed a markedly different specific activity.

In sum, the preparation of Co_3O_4 samples with a hollow nanomorphology through the Kirkendall effect resulted in highly active catalyst for Cl-VOC combustion due to the generation of a large amount of oxygen-vacancy defects on their structure. Thus, the transformation of cobalt acetate hydroxide nanorods precipitated with urea into Co_3O_4 nanotubes following a relatively low-temperature oxidation process regulated by the Kirkendall effect maximised the number of active sites and ultimately optimised the efficiency in the destruction of C_2-chlorinated compounds. Particularly, this sample was characterised by a highly defective structure at surface and bulk levels as suggested by its high Co^{2+}/Co^{3+} molar ratio. Indeed, the observed good correlations of the specific reaction rate with the amount of surface oxygen species (O_2-TPD) and O_{ads}/O_{latt} (XPS) evidenced that oxygen defects at the surface mainly controls the activity of the investigated samples. These findings would be in agreement with a Mars van Krevelen mechanism that assumes that the reaction proceeds between the oxygen-rich sites (adsorbed oxygen species) and adsorbed Cl-VOCs on acid sites.

Activity data were kinetically analysed considering pseudo-first order kinetics in chlorinated VOC, zero order for oxygen (due to its large concentration), and an Arrhenius dependence of the rate constant. These power-law dependences are usually found in the literature for chlorinated VOC combustion, being considered useful for catalyst comparison as well as preliminary reactor design. These requirements were assumed to be valid for the catalytic combustion of chlorinated hydrocarbon-air diluted mixtures over the examined cobalt catalysts. To determine the kinetic parameters (i.e. activation energy and pre-exponential factor) for the catalytic oxidation of the two C_2-chlorinated molecules, the integral method was used. Consequently, if the change in density of the reactant gas due to reaction is considered

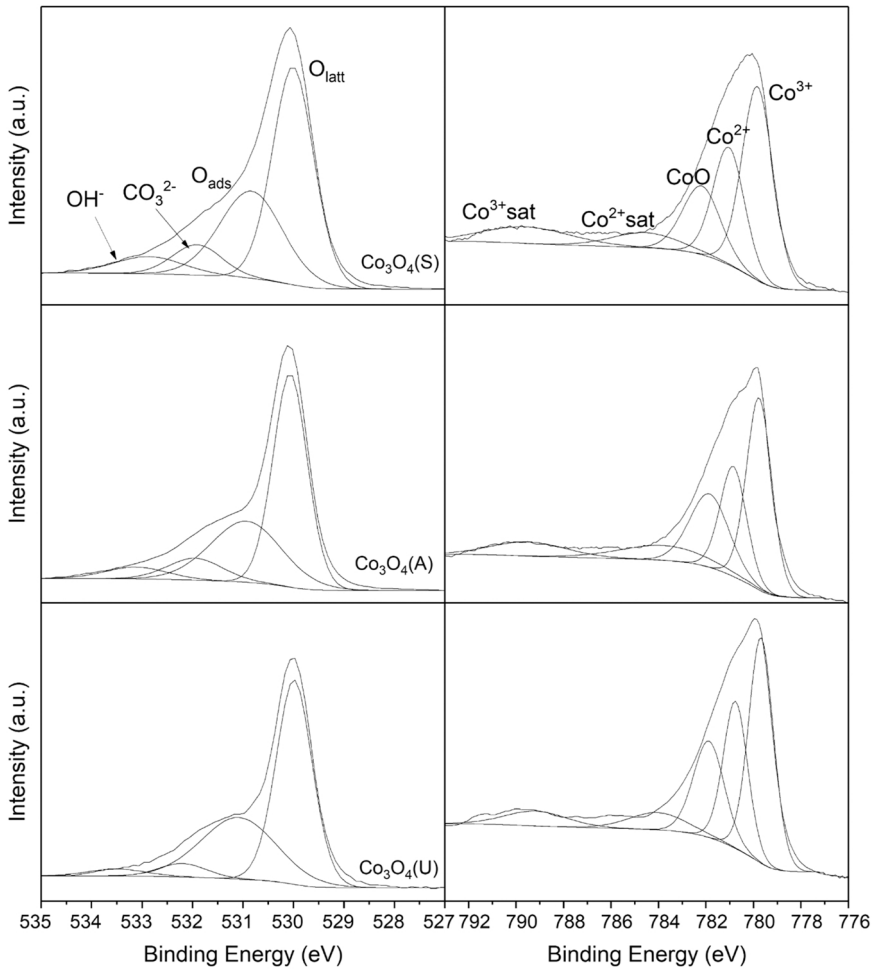

Fig. 7. XPS profiles of the Co_3O_4 catalysts.

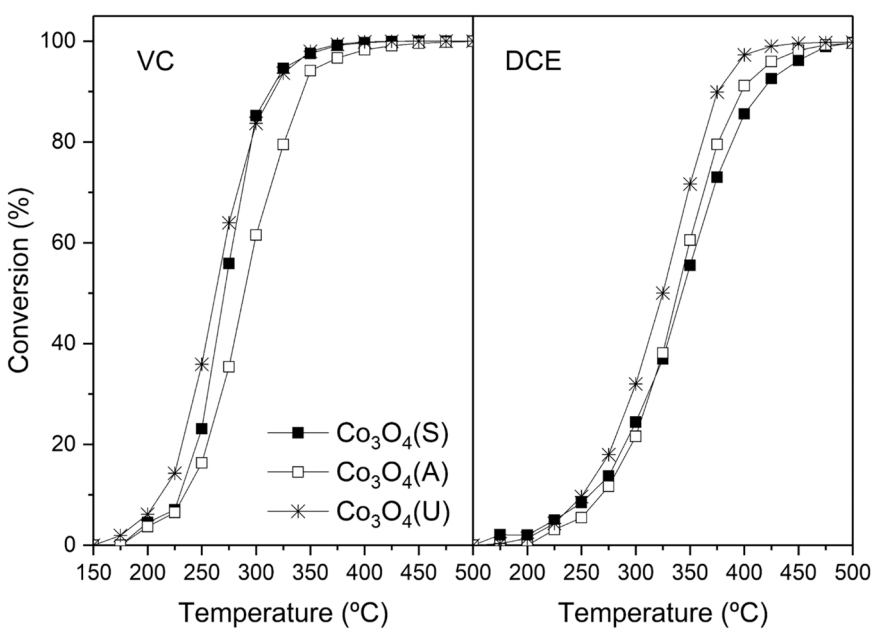

Fig. 8. Light-off curves of the Co_3O_4 catalysts.

Table 3
Kinetic results of the oxidation of VC and DCE over the Co_3O_4 catalysts.

Catalyst	VC					DCE				
	T_{50}, °C	T_{90}, °C	$(-r_A)$, mmol g^{-1} h^{-1}	E_a, kJ mol^{-1}	k_0 ($x10^5$), mol g^{-1} s^{-1} MPa^{-1}	T_{50}, °C	T_{90}, °C	$(-r_A)$, mmol g^{-1} h^{-1}	E_a, kJ mol^{-1}	k_0 ($x10^3$), mol g^{-1} s^{-1} MPa^{-1}
Co_3O_4(S)	270	315	0.18	88	8.72	345	415	0.24	62	0.50
Co_3O_4(A)	290	345	0.11	74	0.21	340	400	0.20	76	8.44
Co_3O_4(U)	265	315	0.23	78	1.04	325	375	0.29	70	4.06

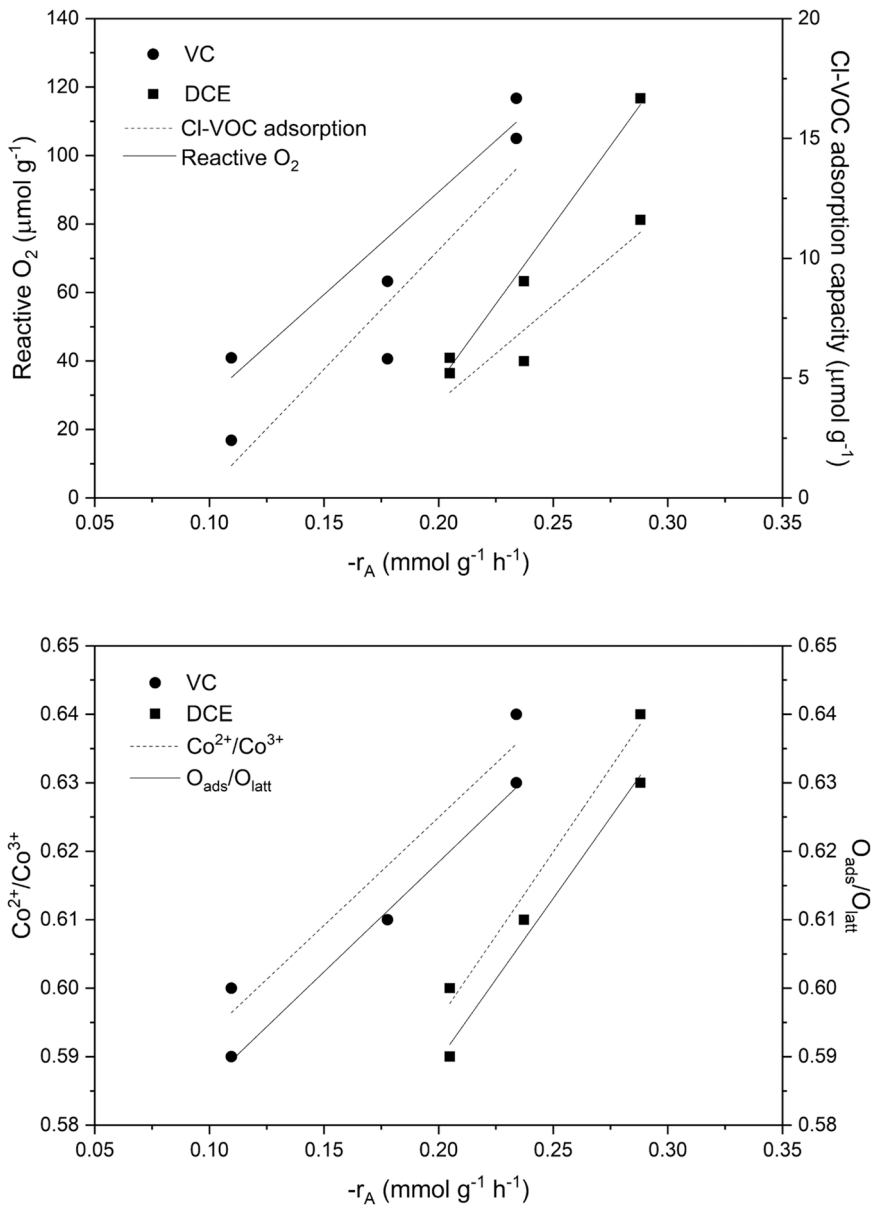

Fig. 9. Relationship among the specific reaction rate, the amount of active oxygen species, the Cl-VOC adsorption capacity and the Co^{2+}/Co^{3+} and O_{ads}/O_{latt} molar ratios.

negligible (since the chlorinated VOC is very diluted), then the following linearised equation could be derived for the integral reactor,

$$\ln[-\ln(1-X)] = \ln[(k_0 P_{Cl-VOC_0}(W/F_{Cl-VOC_0})] - E_a/RT \quad (1)$$

where X is the fractional conversion of the chlorinated VOC, k_0 is the pre-exponential factor of the Arrhenius equation and $W/F_{Cl\text{-}VOC,0}$ is the weight hourly space velocity. Conversions between 5% and 80% were fit to Eq. (1). Pre-exponential factor and apparent activation energy obtained for the cobalt oxide catalysts tested in this work are included in Table 3. The goodness of the numerical fit could be assessed from Fig. 10. The activation energies were quite similar within the experimental error for all the oxide samples. Thus, the values were in the 74–88 kJ mol^{-1} range for VC and 62–76 kJ mol^{-1} range for DCE. This suggested that the reaction mechanism was essentially the same irrespective of the preparation method and the chlorinated molecule. These E_a values were similar with those found in the literature for the

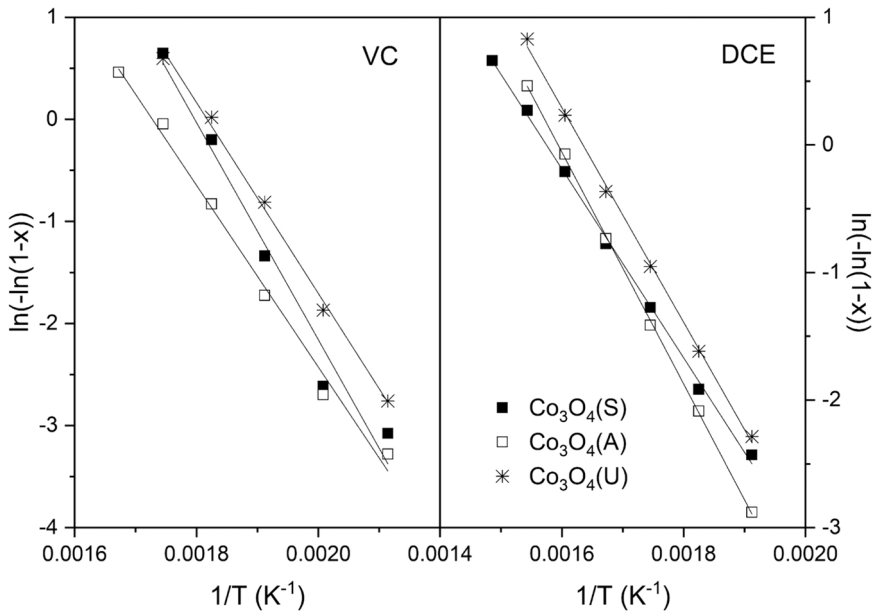

Fig. 10. Pseudo-first order fit for the experimental data obtained over the Co_3O_4 catalysts.

Table 4
Comparison of the activation energies in chlorinated VOC oxidation with metal oxide catalysts reported in the literature.

Catalyst	Chlorinated VOC	Cl-VOC concentration, ppm	WHSV, mL g^{-1} h^{-1}	E_a, kJ mol^{-1}	Reference
Co_3O_4	1,2-dichloroethane	1000	35000	62–76	This work
Co_3O_4	Vinyl chloride	1000	35000	74–88	This work
$10MnO_x/TiO_2$	1,2-dichloroethane	1000	40000	69	[9]
ZrO_2	1,2-dichloroethane	1000	30000	68	[45]
1%Co/HZSM-5	1,2-dichloroethane	1000	20000	70	[46]
Co_3O_4	Vinyl chloride	1000	15000	76–84	[31]
Cr_xTi_{1-x}	Vinyl chloride	1000	30000	62–85	[44]
CoO_x/Al_2O_3-hms	Vinyl chloride	1000	30000	86	[47]

combustion of DCE and VC over Co-, Cr- and Mn-based transition metal oxide catalysts (Table 4) [9,31,44–47]. Fig. S4 (Supplementary Material) shows the relationship between the experimental conversion values and the conversion values dictated by the kinetic model. The results presented in this figure demonstrated that the proposed kinetic rate expression provided an accurate data correlation over the wide range of temperatures investigated (150–500 °C).

As well as a notable activity, that is, a high conversion at the lowest temperatures, the suitability of a catalyst for chlorinated VOC removal is also affected by a limited generation of chlorinated by-products derived from an incomplete conversion of the feed. A high selectivity to CO_2 and HCl/Cl_2 (deep oxidation products) is desired as well. As an example, Fig. 11 shows the product distribution of the oxidation of both pollutants over the most active Co_3O_4 catalyst (Co_3O_4(U)). Fig. S5 (Supplementary Material) includes the corresponding distribution over the other two examined samples (Co_3O_4(S) and Co_3O_4(A)). It was observed that the main oxidation products were CO_2, HCl and Cl_2. It is worth noting that the formation of CO was always negligible. Interestingly, relatively reduced amounts of chlorinated by-products were also observed. In both Fig. (11 and S5) the evolution of the accumulated profiles of these by-products is included. The peak concentration (at 275 °C for VC and at 325 °C for DCE) was always lower than 200 ppm. Fig. S6 (Supplementary Material) more explicitly includes the chemical nature of the observed by-products. In the case of VC several chlorinated methanes were detected, namely dichloromethane (25 ppm), trichloromethane (35 ppm) and tetrachloromethane (70 ppm). This by-product distribution was in agreement with the results by Wang et al. [48] who observed 1,1,2-trichloroethane, dichloromethane, trichloromethane and tetrachloromethane as the major chlorinated by-products during the oxidation of VC over Ru modified Co_3O_4 catalysts. 1,1,2-trichloroethane might be generated from the addition reaction between VC and surface active chlorine species, and subsequently be cracked into dichloromethane and trichloromethane that could lead to the generation of tetrachloromethane by further chlorination. As for DCE, in addition to chlorinated methanes (dichloromethane (15 ppm), trichloromethane (25–45 ppm) and tetrachloromethane (25–50 ppm)), chlorinated ethylenes were also formed (vinyl chloride (20–30 ppm) and cis-1, 2-dichloroethylene (10–30 ppm)). While vinyl chloride is expected to be formed due to dehydrochlorination of the feed on the acid sites of the catalyst and may undergo chlorination leading to the formation of cis- and trans-1,2-dichloroethylene isomers, the generation of the other highly chlorinated compounds was associated with (oxy)chlorination reactions of DCE [6,28]. The main chlorinated deep oxidation products were HCl and Cl_2. The generation of molecular chlorine was ascribed to the occurrence of the Deacon reaction ($2HCl + 1/2\ O_2 \rightarrow Cl_2 + H_2O$), which was activated with increased temperature. Under full Cl-VOC conversion conditions over the Co_3O_4(U) catalyst (325 °C for VC and 375 °C for DCE) the observed HCl/Cl_2 molar ratio was 2.3 (VC) and 1.3 (DCE).

3.3. Catalytic stability and durability

The catalytic stability of the most efficient Co_3O_4, namely Co_3O_4(U) hollow nanotubes, was investigated by analysing the evolution of conversion to CO_2 with time on stream at constant temperature. Given its most recalcitrant character, DCE was selected for this study. In order to

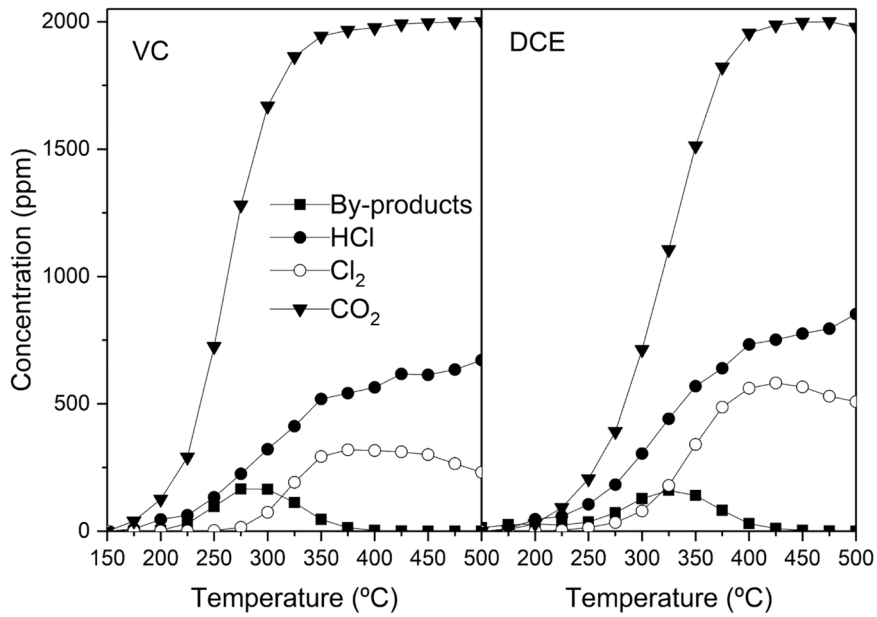

Fig. 11. Product distribution during the catalytic oxidation of DCE and VC over the Co_3O_4(U) catalyst.

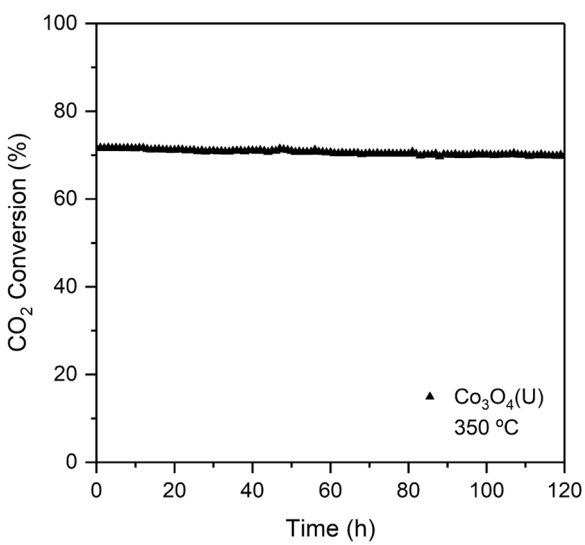

Fig. 12. Stability in DCE oxidation at 350 °C over the Co_3O_4(U) catalyst for 120 h.

provide a more sensitive indication of changes of the catalyst performance with time on line (120 h), a temperature of 350 °C was selected as it provoked a conversion markedly below 100%. Results included in Fig. 12 showed that conversion remained stable (70%) with no appreciable deactivation. This notable stability evidenced that the population of active sites was not significantly modified. As for the other two less active Co_3O_4 catalysts, it should be pointed out that, although their long term durability was not examined, they were submitted to two consecutive light-off tests with each chlorinated VOC (VC and DCE) with an accumulated reaction time interval of 20 h. No marked differences in behaviour were found, thereby suggesting a good stability as well. The used Co_3O_4(U) catalyst was characterised by N_2 physisorption, XRD, EDS, and temperature-programmed oxidation (TPO). The surface area decreased by 15% (from 19 to 16 $m^2\ g^{-1}$), whereas the Co_3O_4 crystallite size remained almost unaltered (24 vs 22 nm for the fresh oxide). Moreover, no diffraction peaks corresponding to the formation of less active CoO were noted. EDS analysis revealed the presence of small amounts of chlorine (0.35 wt%) on the sample. Likewise, traces of carbonaceous deposits, which could be originated by DCE cracking/polymerisation [38], were detected (0.35 wt%), as evidenced by TPO measurements. Judging from these results it was reasonable to expect that these small changes barely affected the behaviour of the optimal Co_3O_4 catalyst.

4. Conclusions

A series of nanostructured (hollow nanotubes) bulk cobalt oxide catalysts were synthesised following preparation routes based on the Kirkendall effect. The prepared samples were thoroughly characterised (N_2 physisorption, XRD, SEM-EDX, H_2-TPR, O_2-TPD, adsorption of ammonia and chlorinated VOC followed by thermogravimetry, XPS, Raman spectroscopy and TPO) and evaluated for complete oxidation of vinyl chloride and 1,2-dichloroethane. The catalytic performance of the as-prepared hollow nanotubes was synergically governed by a combination of features that included a large surface area, a relatively low crystallite size, a high population of Co^{2+} species at bulk and surface level, which in turn maximised the amount of active surface oxygen species, and a high affinity for efficient chemisorption of the chlorinated VOC. Hence, the nanotubes prepared from cobalt acetate in the presence of urea submitted to a controlled thermal activation resulted in the most active Co_3O_4 catalyst for the efficient oxidation of both C_2-chlorinated pollutants, with an excellent selectivity to deep combustion products (CO_2, HCl and Cl_2) at 315 and 375 °C. Furthermore, this sample exhibited a notable stability during a relatively prolonged time on stream (120 h) with no clear evidence of deactivation due to a good preservation of the physico-chemical properties and a minimal accumulation of coke and chlorine species on the surface.

CRediT authorship contribution statement

Amaya Gil-Barbarin: Investigation, Writing – original draft, Formal analysis. **Jose Ignacio Gutiérrez-Ortiz:** Methodology, Formal analysis, Funding acquisition. **Rubén López-Fonseca:** Conceptualization, Writing – review & editing, Funding acquisition, Project administration. **Beatriz de Rivas:** Methodology, Formal analysis, Validation, Writing – review & editing, Supervision.

Declaration of Competing Interest

In this work, we have tried to understand the chemical and structural nature of Co_3O_4 hollow nanotubes following preparation routes based on the Kirkendall effect, and to establish a link between the catalyst properties and its kinetic behaviour for C_2-chlorinated VOC oxidation. The catalytic performance of the as-prepared nanotubes was synergically governed by a combination of features that included a large surface area, a relatively low crystallite size, a high population of Co^{2+} species at bulk and surface level, which in turn maximised the amount of active surface oxygen species, and a high affinity for efficient chemisorption of the chlorinated VOC.

Data Availability

Data will be made available on request.

Acknowledgments

This research was funded by the Spanish Ministry of Science and Innovation (PID2019-107105RB-I00 AEI/FEDER, UE and PDC2022-133897-I00), the Basque Government (IT1509-22), and the University of the Basque Country UPV/EHU (PIF18/185). The authors are grateful for the technical and personal support provided by SGIker (UPV/EHU). In addition, the authors acknowledge the use of instrumentation as well as the technical advice provided by the National Facility ELECMI ICTS, node "Advanced Microscopy Laboratory" at the University of Zaragoza.

Appendix A. Supporting information

Supplementary data associated with this article can be found in the online version at doi:10.1016/j.jece.2023.109841.

References

[1] B. Huang, C. Lei, C. Wei, G. Zeng, Chlorinated volatile organic compounds (Cl-VOCs) in environment—sources, potential human health impacts, and current remediation technologies, Environ. Int. 71 (2014) 118–138, https://doi.org/10.1016/j.envint.2014.06.013.

[2] C. Dai, Y. Zhou, H. Peng, S. Huang, P. Qin, J. Zhang, Y. Yang, L. Luo, X. Zhang, Current progress in remediation of chlorinated volatile organic compounds: a review, J. Ind. Eng. Chem. 62 (2018) 106–119, https://doi.org/10.1016/j.jiec.2017.12.049.

[3] F. Lin, L. Xiang, Z. Zhang, N. Li, B. Yan, C. He, Z. Hao, G. Chen, Comprehensive review on catalytic degradation of Cl-VOCs under the practical application conditions, Crit. Rev. Environ. Sci. Tec. (2020) 311–355, https://doi.org/10.1080/10643389.2020.1818490.

[4] E. Dobrzynska, M. Posniak, M. Szewczynska, B. Buszewski, Chlorinated volatile organic compounds – old, however, actual analytical and toxicological problem, Crit. Rev. Anal., Chem. 40 (2010) 41–57, https://doi.org/10.1080/10408340903547054.

[5] A.M. Evuti, A synopsis on biogenic and anthropogenic volatile organic compounds emissions: hazards and control, Int. J. Eng. Sci. 2 (2013) 145–153.

[6] F. Lin, Z. Zhang, N. Li, B.B. Yan, C. He, Z. Hao, G. Chen, How to achieve complete elimination of Cl-VOCs: a critical review on byproducts formation and inhibition strategies during catalytic oxidation, Chem. Eng. J. 404 (2021), 126534, https://doi.org/10.1016/j.cej.2020.126534.

[7] M.S. Kamal, S.A. Razzak, M.M. Hossain, Catalytic oxidation of volatile organic compounds (VOCs) – a review, Atmos. Environ. 140 (2016) 117–134, https://doi.org/10.1016/j.atmosenv.2016.05.031.

[8] Q. Dai, S. Bai, H. Li, W. Liu, X. Wang, G. Lu, Catalytic total oxidation of 1,2-dichloroethane over highly dispersed vanadia supported on CeO_2 nanobelts, Appl. Catal. B-Environ. 168- 169 (2015) 141–155, https://doi.org/10.1016/j.apcatb.2014.12.028.

[9] X. Zhang, Y. Liu, J. Deng, L. Jing, X. Yu, Z. Han, H. Dai, Effect on transition metal oxide doping on catalytic activity of titania for the oxidation of 1,2-dichloroethane, Catal. Today 375 (2021) 623–634, https://doi.org/10.1016/j.cattod.2019.12.011.

[10] C. Zhang, C. Wang, W. Hua, Y. Guo, G. Lu, S. Gil, A. Giroir-Fendler, Relationship between catalytic deactivation and physicochemical properties of $LaMnO_3$ perovskite catalyst during catalytic oxidation of vinyl chloride, Appl. Catal. B-Environ. 186 (2016) 173–183, https://doi.org/10.1016/j.apcatb.2015.12.052.

[11] A. Choya, B. de Rivas, J.R. González-Velasco, J.I. Gutiérrez-Ortiz, R. López-Fonseca, Oxidation of residual methane from VNG vehicles over Co_3O_4-based catalysts: comparison among bulk, Al_2O_3-supported and Ce-doped catalysts, Appl. Catal. B-Environ. 237 (2018) 844–854, https://doi.org/10.1016/j.apcatb.2018.06.050.

[12] L. Ma, W. Zhang, Y.G. Wang, X. Chen, W. Yu, K. Sun, H. Sun, J. Li, J.W. Schwank, Catalytic performance and reaction mechanism of NO oxidation over Co_3O_4 catalysts, Appl. Catal. B-Environ. 267 (2020), 118371, https://doi.org/10.1016/j.apcatb.2019.118371.

[13] J. Liu, C. Zhou, W. Yue, B. Yan, Y. Lin, A. Huang, Facile and green template-free synthesis of morphology-controllable Co_3O_4 catalysts for CO oxidation, Chem. Phys. Lett. 756 (2020), 137817, https://doi.org/10.1016/j.cplett.2020.137817.

[14] Q. Liu, L.C. Wang, M. Chen, Y. Cao, H.Y. He, K.N. Fan, Dry citrate-precursor synthesized nanocrystalline cobalt oxide as highly active catalyst for total oxidation of propane, J. Catal. 263 (2009) 104–113, https://doi.org/10.1016/j.jcat.2009.01.018.

[15] X. Zhu, B. Bai, B. Zhou, S. Ji, Co_3O_4 nanoparticles with different morphologies for catalytic removal of ethyl acetate, Catal. Commun. 156 (2021), 106320, https://doi.org/10.1016/j.catcom.2021.106320.

[16] W. Liu, R. Liu, H. Zhang, Q. Jin, Z. Song, W. Zhang, Fabrication of Co_3O_4 nanospheres and their catalytic performances for toluene oxidation: the distinct effects of morphology and oxygen species, Appl. Catal. A-Gen. 597 (2020), 117539, https://doi.org/10.1016/j.apcata.2020.117539.

[17] Z. Wang, R. Yu, Hollow micro/nanostructured ceria-based materials: synthetic strategies and versatile applications, Adv. Mater. 31 (2019) 1800592, https://doi.org/10.1002/adma.201800592.

[18] M. Zhang, S. Zou, Q. Zhang, S. Mo, J. Zhong, D. Chen, M. Fu, P. Chen, D. Ye, Macroscopic hexagonal Co_3O_4 tubes derived from controllable two-dimensional metal-organic layer single crystals: formation, mechanism and catalytic activity, Inorg. Chem. 59 (2020) 3062–3071, https://doi.org/10.1021/acs.inorgchem.9b03396.

[19] J. Zhong, Y. Zeng, M. Zhang, W. Feng, D. Xiao, J. Wu, P. Chen, M. Fu, D. Ye, Toluene oxidation process and proper mechanism over Co_3O_4 nanotubes: investigation through in-situ DRIFTS combined with PTR-TOF-MS and quasi in-situ XPS, Chem. Eng. J. 397 (2020), 125375, https://doi.org/10.1016/j.cej.2020.125375.

[20] C. Yuan, H.G. Wang, J. Liu, Q. Wu, Q. Duan, Y. Li, Facile synthesis of Co_3O_4-CeO_2 composite oxide nanotubes and their multifunctional applications for lithium ion batteries and CO oxidation, J. Colloid Interface Sci. 494 (2017) 274–281, https://doi.org/10.1016/j.jcis.2017.01.074.

[21] Z. Fei, S. He, L. Li, W. Ji, C.T. Au, Morphology-directed synthesis of Co_3O_4 nanotubes based on modified Kirkendall effect and its application in CH_4 combustion, Chem. Commun. 48 (2012) 853–855, https://doi.org/10.1039/C1CC15976C.

[22] Y. Lv, Y. Li, W. Shen, Synthesis of Co_3O_4 nanotubes and their catalytic applications in CO oxidation, Catal. Commun. 42 (2013) 116–120, https://doi.org/10.1016/j.catcom.2013.08.017.

[23] United States Environmental Protection Agency (US EPA). Vinyl chloride: national emission standards for hazardous air pollutants (NESHAP). https://www.epa.gov/stationary-sources-air-pollution/vinyl-chloride-national-emission-standards-hazardous-air-pollutants, 2022 (accessed 7 November 2022).

[24] Z. Huang, Y. Zhao, Y. Song, Y. Lu, Y. Li, G. Wu, H. Tang, J. Zhao, Solution inheritance of $CoC_2O_4{\cdot}2H_2O$ rods to nanoparticle-assembled Co_3O_4 rods, Colloid Surf. A. 490 (2016) 307–317, https://doi.org/10.1016/j.colsurfa.2015.11.064.

[25] S. Wang, C. Xiao, P. Wang, Z. Li, B. Xiao, R. Zhao, T. Yang, M. Zhang, Co_3O_4 hollow nanotubes: facile synthesis and gas sensing properties, Mater. Lett. 137 (2014) 289–292, https://doi.org/10.1016/j.matlet.2014.09.021.

[26] D. Ge, Y. Yang, X. Ni, J. Dong, Q. Qiu, X.Q. Chu, X. Chen, Self-template formation of porous Co_3O_4 hollow nanoprisms for non-enzymatic glucose sensing in human serum, RSC Adv. 10 (2020) 38369, https://doi.org/10.1039/D0RA06453J.

[27] R. López-Fonseca, S. Cibrián, J.I. Gutiérrez-Ortiz, M.A. Gutiérrez-Ortiz, J. R. González-Velasco, Oxidative destruction of dichloromethane over protonic zeolites, AIChe J. 49 (2003) 496–504, https://doi.org/10.1002/aic.690490219.

[28] J. González-Prior, J.I. Gutiérrez-Ortiz, R. López-Fonseca, G. Busca, E. Finocchio, B. de Rivas, Oxidation of chlorinated alkanes over Co_3O_4 SBA-15 catalysts. Structural characterization and reaction mechanism, Catal. Sci. Technol. 6 (2016) 5618–5630, https://doi.org/10.1039/C6CY00321D.

[29] Y. Zhang, Y. Chen, T. Wang, J. Zhou, Y. Zhao, Synthesis and magnetic properties of nanoporous Co_3O_4 nanoflowers, Micro Mesopor. Mat. 114 (2008) 257–261, https://doi.org/10.1016/j.micromeso.2008.01.011.

[30] W. Du, R. Liu, Y. Jiang, Q. Lu, Y. Fan, F. Gao, Facile synthesis of hollow Co_3O_4 boxes for high capacity supercapacitor, J. Power Sources 227 (2013) 101–105, https://doi.org/10.1016/j.jpowsour.2012.11.009.

[31] W.C. Hua, M.Q. Li, Y.L. Guo, G.T. Chai, H. Liu, Y. Guo, L. Wang, W.C. Zhan, Catalytic combustion of vinyl chloride emissions over Co_3O_4 catalysts with different crystallite sizes, Rare. Met. 40 (2021) 817–827, https://doi.org/10.1007/s12598-020-01512-3.

[32] B. de Rivas, R. López-Fonseca, C. Jiménez-González, J.I. Gutiérrez-Ortiz, Highly active behaviour of nanocrystalline Co_3O_4 from oxalate nanorods in the oxidation of chlorinated short chain alkanes, Chem. Eng. J. 184 (2012) 184–192, https://doi.org/10.1016/j.cej.2012.01.027.

[33] J. González-Prior, R. López-Fonseca, J.I. Gutiérrez-Ortiz, B, Oxidation of 1,2-dichloroethane over nanocube-shaped Co_3O_4 catalysts, Catal. B-Environ. 199 (2016) 384–393, https://doi.org/10.1016/j.apcatb.2016.06.046.

[34] G. Chai, D. Du, C. Wang, C. Zhang, L. Cardenas, N. Bion, Y. Guo, S. Gil, A. Giroir-Fendler, Spinel Co_3O_4 oxides-support synergistic effect on catalytic oxidation of toluene, Appl. Catal. A-Gen. 614 (2021), 118044, https://doi.org/10.1016/j.apcata.2021.118044.

[35] P.L. Meena, R. Kumar, K. Sreenivas, Structural, elastic and magnetic properties of spinel Co_3O_4, Indian J. Pure Appl. Phys. 56 (2018) 890–895.
[36] B. de Rivas, R. López-Fonseca, C. Jiménez-González, J.I. Gutiérrez-Ortiz, Synthesis, characterisation and catalytic performance of nanocrystalline Co_3O_4 for gas-phase chlorinated VOC abatement, J. Catal. 281 (2011) 88–97, https://doi.org/10.1016/j.jcat.2011.04.005.
[37] W. Song, A.S. Poyraz, Y. Meng, Z. Ren, S.Y. Chen, S.L. Suib, Mesoporous Co_3O_4 with controlled porosity: inverse micelle synthesis and high-performance catalytic CO oxidation at -60 °C, Chem. Mater. 26 (2014) 4629–4639, https://doi.org/10.1021/cm502106v.
[38] J. González-Prior, R. López-Fonseca, J.I. Gutiérrez-Ortiz, B. de Rivas, Catalytic removal of chlorinated compounds over ordered mesoporous cobalt oxides synthesised by hard-templating, Appl. Catal. B-Environ. 222 (2018) 9–17, https://doi.org/10.1016/j.apcatb.2017.09.050.
[39] K. Shojaee, B.S. Haynes, A. Montoya, The catalytic oxidation of NH_3 on Co_3O_4 (110): a theoretical study, P. Combust. Inst. 36 (2017) 4365–4373, https://doi.org/10.1016/j.proci.2016.06.100.
[40] X. Feng, J. Guo, X. Wen, M. Xu, Y. Chu, S. Yuan, Enhancing performance of Co/CeO_2 catalyst by Sr doping for catalytic combustion of toluene, Appl. Surf. Sci. 445 (2018) 145–153, https://doi.org/10.1016/j.apsusc.2018.03.070.
[41] Y. Su, H. Liu, C. Li, J. Liu, Y. Song, F. Wang, Hydrothermal-assisted defect engineering in spinel Co_3O_4 nanostructures as bifunctional catalysts for oxygen electrode, J. Alloy. Compd. 799 (2019) 160–168, https://doi.org/10.1016/j.jallcom.2019.05.331.
[42] J.C. Dupin, D. Gonbeau, P. Vinatier, A. Levasseur, Systematic XPS studies of metal oxides, hydroxides and peroxides, Phys. Chem. Chem. Phys. 2 (2000) 1319–1324, https://doi.org/10.1039/A908800H.
[43] K. Zeng, X. Li, C. Wang, Z. Wang, P. Guo, J. Yu, C. Zhang, X.S. Zhao, Three-dimensionally microporous $MnZrO_x$ catalysts for propane combustion: synergistic structure and doping effects on physicochemical and catalytic properties, J. Colloid Interf. Sci. 572 (2020) 281–296, https://doi.org/10.1016/j.jcis.2020.03.093.
[44] W. Sun, B. Gong, J. Pan, Y. Wang, H. Xia, H. Zhang, Q. Dai, L. Wang, X. Wang, Catalytic combustion of CVOCs over Cr_xTi_{1-x} oxide catalysts, J. Catal. 391 (2020) 132–144, https://doi.org/10.1016/j.jcat.2020.08.007.
[45] G. Chen, D. Hong, H. Xia, W. Sun, S. Shao, B. Gong, S. Wang, J. Wu, X. Wang, Q. Dai, Amorphous and homogeneously Zr-doped MnO_x with enhanced acid and redox properties for catalytic oxidation of 1,2-dichloroethane, Chem. Eng. J. 428 (2022), 131067, https://doi.org/10.1016/j.cej.2021.131067.
[46] X. Zhang, L. Dai, Y. Liu, J. Deng, L. Jing, Z. Wang, W. Pei, X. Yu, J. Wang, H. Dai, Effect of support nature on catalytic activity of the bimetallic RuCo nanoparticles for the oxidative removal of 1,2-dichloroethane, Appl. Catal. B-Environ. 285 (2021), 119804, https://doi.org/10.1016/j.apcatb.2020.119804.
[47] C. Wang, N. Liu, C. Zhang, X. Liu, X. Li, X.S. Zhao, Ruthenium/cobalt binary oxides supported on hollow alumina microspheres as highly efficient catalyst for vinyl chloride oxidation, Appl. Surf. Sci. 497 (2019), 143776, https://doi.org/10.1016/j.apsusc.2019.143776.
[48] C. Wang, C. Zhang, W. Hua, Y. Guo, G. Lu, S. Gil, A. Giroir-Fendler, Low-temperature catalytic oxidation of vinyl chloride over Ru modified Co_3O_4 catalyst, RSC Adv. 6 (2016) 99577–99585, https://doi.org/10.1039/C6RA18503G.